AN ANALYSIS OF THE SHAPES OF INTERSTELLAR EXTINCTION CURVES. VI. THE NEAR-IR EXTINCTION LAW

E. L. FITZPATRICK[1] AND D. MASSA[2]

[1] Department of Astronomy & Astrophysics, Villanova University, 800 Lancaster Avenue, Villanova, PA 19085, USA; edward.fitzpatrick@villanova.edu
[2] SGT, Inc., Space Telescope Science Institute, 3700 San Martin Dr., Baltimore, MD 21218, USA; massa@derckmassa.net

ABSTRACT

We combine new observations from the *Hubble Space Telescope*'s Advanced Camera of Survey with existing data to investigate the wavelength dependence of near-IR (NIR) extinction. Previous studies suggest a power law form for NIR extinction, with a "universal" value of the exponent, although some recent observations indicate that significant sight line-to-sight line variability may exist. We show that a power-law model for the NIR extinction provides an excellent fit to most extinction curves, but that the value of the power, β, varies significantly from sight line to sight line. Therefore, it seems that a "universal NIR extinction law" is not possible. Instead, we find that as β decreases, $R(V) \equiv A(V)/E(B-V)$ tends to increase, suggesting that NIR extinction curves which have been considered "peculiar" may, in fact, be typical for different $R(V)$ values. We show that the power-law parameters can depend on the wavelength interval used to derive them, with the β increasing as longer wavelengths are included. This result implies that extrapolating power-law fits to determine $R(V)$ is unreliable. To avoid this problem, we adopt a different functional form for NIR extinction. This new form mimics a power law whose exponent increases with wavelength, has only two free parameters, can fit all of our curves over a longer wavelength baseline and to higher precision, and produces $R(V)$ values which are consistent with independent estimates and commonly used methods for estimating $R(V)$. Furthermore, unlike the power-law model, it gives $R(V)$s that are independent of the wavelength interval used to derive them. It also suggests that the relation $R(V) = -1.36 \frac{E(K-V)}{E(B-V)} - 0.79$ can estimate $R(V)$ to ± 0.12. Finally, we use model extinction curves to show that our extinction curves are in accord with theoretical expectations, and demonstrate how large samples of observational quantities can provide useful constraints on the grain properties.

Key words: dust, extinction

1. INTRODUCTION

In the previous papers in this series, we began with an in-depth look at the structure and properties of UV extinction curves, including the 2175 Å "bump" (Fitzpatrick & Massa 1986, 1988, 1990), and most recently completed a general survey of Galactic extinction covering the near-IR (NIR) through UV spectral regions (Fitzpatrick & Massa 2005a, 2007, hereafter Papers IV and V, respectively). These studies have utilized Two-Micron All Sky Survey (2MASS) *JHK* photometry, optical photometry, and low-resolution *International Ultraviolet Explorer* satellite (*IUE*) spectrophotometry. Our general goal of codifying the behavior of interstellar extinction over the widest possible wavelength range has been motivated by two scientific objectives: (1) to aid in the identification of the dust grain populations which produce the extinction and (2) to provide tools for the removal of the effects of wavelength-dependent extinction from astronomical data.

During the course of this study, it has become clear that our ability to characterize extinction properties is strongly limited by the non-uniform type and quality of the data available in the various spectral domains. In fact, due to the success of the *IUE* mission, the best characterized extinction curves are in the once-inaccessible UV region (1200–3000 Å), while the worst characterized regions are the "gaps" between UV and optical data (∼3000–3800 Å) and between IR and optical data (∼6000–10000 Å). These regions are, in principle, accessible from the ground but, due to calibration issues, remain poorly studied. In an attempt to remedy this situation, we obtained spectrophotometric data from the Advanced Camera for Surveys (ACS) aboard the *Hubble Space Telescope* (*HST*). The observations included both gap regions, although for reasons discussed in

Section 2.1 below, only the data spanning the optical-IR gap were useful for the program. These data, however, turn out to be of value not only for characterizing the wavelength dependence of extinction along the chosen set of sight lines, but also for addressing the broader issue of a "universal" extinction law in the IR region. A variety of observations have suggested a common form to extinction at wavelengths from the *I* band through ∽5 μm (e.g., Rieke & Lebofsky 1985; Martin & Whittet 1990), consistent with a power law form for the extinction law, $A_\lambda \propto \lambda^{-\beta}$, and an exponent value of $\beta = 1.84$ for both diffuse and dark cloud lines of sight (Whittet 2003). More recent observations, however, have suggested significant sight line-to-sight line variability in IR extinction with a potentially large range of power-law exponents (Larson & Whittet 2005; Nishiyama et al. 2006; Froebrich et al. 2007; Gosling et al. 2009).

In this paper, we use our new ACS observations in the gap region between the optical and the NIR, along with existing data, to investigate the shape of the extinction law in this region and also the issue of whether a universal NIR law exists. In Section 2, the target stars and the data used here (both new and archival) are described. In Section 3, we discuss the technique used to derive extinction curves, and consider two families of analytic functions that can be used to represent them. In Section 4, we examine how our results compare to theoretical models. Section 5 summarizes the main results of the paper and an Appendix addresses technical issues concerning the ACS calibration.

2. THE TARGET STARS AND THEIR DATA

In this study, we examine extinction curves toward 14 stars drawn from a set of more than 300 stars studied in

Table 1
The Target Stars and the New *HST*/ACS G800L Data

Star	Spectral Type[a]	V[a]	$E(B-V)$[a]	ACS Data Sets	Observation Dates
BD+56 517	B1.5 V	10.50	0.51	J9FH34041, J9FH34051	2005 Aug 2
BD+45 973	B3 V	8.58	0.80	J9FH30041, J9FH30051	2005 Sep 1
BD+44 1080	B6 III	9.12	0.99	J9FH29041, J9FH29051	2005 Aug 22
NGC 1977 #885	B4 V	11.33	0.82	J9FH15041, J9FH15051	2005 Oct 10
HD 46106	B1 V	7.92	0.43	J9FH38041, J9FH38051	2005 Oct 19
HD 292167	O9 III:	9.25	0.72	J9FH27041, J9FH27051	2005 Sep 3
HD 68633	B5 V	9.91	0.49	J9FH17041, J9FH17051	2006 Apr 23
HD 70614	B6	9.27	0.68	J9FH18041, J9FH18051	2006 Sep 21
Trumpler 14 #6	B1 V	11.23	0.48	J9FH52041, J9FH52051	2005 Nov 6
Trumpler 14 #27	⋯	11.30	0.58	J9FH51041, J9FH51051	2005 Aug 11
HD 164740	O7.5 V(n)	10.30	0.86	J9FH08041, J9FH08051	2005 Aug 19
HD 229196	O6 III(n)(f)	8.52	1.20	J9FH23041, J9FH23051	2006 Mar 14
HD 204827	B0 V	7.94	1.08	J9FH11041, J9FH11051	2005 Aug 2
BD+61 2365	B0.5 V	9.19	0.78	J9FH42041, J9FH42051	2005 Dec 22

Note.
[a] Spectral types, *V* magnitudes, and $E(B-V)$ values are taken from Paper V; references for the spectral types are given in that paper.

Paper V. These 14 stars, along with their spectral types, *V* magnitudes, and reddenings, are listed in Table 1. Since our method for deriving extinction curves involves modeling the observed spectral energy distributions (SEDs) of reddened stars—using stellar atmosphere calculations and an analytical form of the extinction curve—we require absolutely calibrated photometry and spectrophotometry. The observing program and the processing of the new *HST*/ACS data are described in Section 2.1. The other data sets utilized here (via the analysis in Paper V) are described in Section 2.2, and the complete energy distributions are presented in Section 2.3.

2.1. New ACS Observations

The new observations were part of our Cycle 14 *HST*/ACS program entitled "A SNAP Program to Obtain Complete Wavelength Coverage on Interstellar Extinction." Our goal was to obtain ACS High Resolution Camera (HRC) spectra in the near-UV (using the PR200L grating) and in the NIR (using the GR800L). These data, when combined with existing NIR (*JHK*) photometry, optical photometry, and *IUE* UV spectrophotometry, would provide complete extinction curves over the range ∼1150 Å to ∼2.2 μm. We submitted a target list of 50 stars drawn from the sample in Paper V. Ultimately, 22 stars were observed during 2005 and 2006 and, of these, 14 were deemed suitable for this study. The ACS data were processed and calibrated using the aXe Spectral Extraction package (version 1.6), developed by M. Kümmel, J. Walsh, and H. Kuntschner. We obtained the package from the *HST* European Web site.[3] The aXe software was run in conjunction with the IRAF/PYRAF package on a Sun Microsystems SunBlade1000 machine.

Obtaining absolutely calibrated spectrophotometry with the ACS is a challenging process in general, and for our HRC/PR200L observations it proved to be impossible. The problem was the "red pile-up" effect whereby all photons between 4000 and 10000 Å are focused onto a region of the detector only seven pixels wide (Larsen et al. 2006). This is particularly troublesome for red objects, such as our reddened targets, since diffraction spikes from the resultant bright spot overlap the blue

region of the spectra. We found it impossible to extract reliably uncontaminated spectra from our HRC/PR200L observations and ultimately excluded these data—and consideration of the UV-visual extinction gap—from this study.

Processing the HRC/G800L observations was more straightforward, and we followed the procedures outlined in the aXe Users Manual using an extraction slit height of ±20 pixels. The result was a set of absolutely calibrated first-order grism spectra for our 14 targets covering the range 5700–10200 Å. Because absolute calibration is critical to our program, we also verified the HRC/G800L calibration by examining the HRC/G800L spectra of three DA white dwarf stars used to establish the calibration. We found a significant systematic discrepancy between the calibration targets processed by aXe and their corresponding model atmospheres. Consequently, we had to derive a correction factor for our spectra. This calibration correction is provided in the Appendix. The final step in our ACS data processing was to trim the spectra to the wavelength range 6000–9500 Å, where the fluxes are most reliable.

The final set of 14 ACS/HRS/G800L spectra for our program stars is shown in Figure 1. The spectra have been shifted vertically for clarity. At the top of the figure, the SED of an ATLAS9 (Kurucz 1991) model atmosphere with $T_{\text{eff}} =$ 20,000 K, $\log g = 4.0$, and $[m/\text{H}] = 0$ is shown for comparison. The model fluxes were computed in 20 Å bins in the spectral range shown and smoothed by two points to approximate the two-pixel resolution of the ACS data (i.e., ∼48 Å). While our program stars span a relatively wide range in T_{eff} (∼15,000–40,000 K), the model SED shown provides a reasonable depiction of the stellar features expected in our stars. The H I Hα line at 6563 Å and the upper H I Paschen lines near 9000 Å are the only spectral features of note for our targets and, at the resolution of the HRC/G800L, these features are very weak and generally undetectable. An examination of the individual spectra shows no signs of the H I lines, although numerous low-amplitude "bumps and wiggles" are present. These are instrumental features whose strength and location depend sensitively on the position of the stellar spectrum on the ACS detector. In the discussions to come, these features are smoothed out or eliminated so as not to influence the analysis.
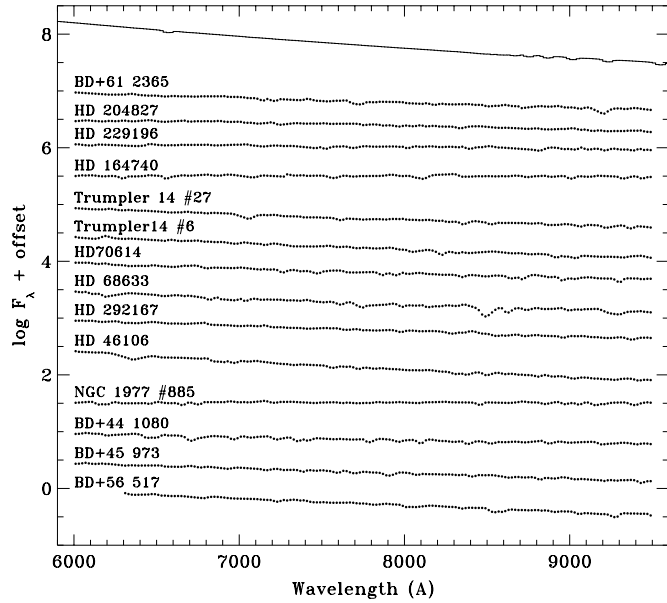
---

[3] www.stecf.org/software/slitless_software/axe/

Figure 1. Final processed ASC/HRC G800L spectra for the 14 program stars. A Kurucz ATLAS9 model with $T_{\rm eff} = 20,000$ K is shown near the top of the figure for comparison. Weak Hα and H I Paschen absorption lines may be present in our spectra, although they would be close to the detection limit. All the prominent "bumps and wiggles" seen in the ACS spectra are instrumental in the origin.

2.2. Other Data

As will be described in Section 3, we will use the SED-fitting results from Paper V, and thus implicitly rely on the data used there. These included low-resolution UV spectrophotometry from the *IUE* satellite, obtained via the Multimission Archive at STScI (MAST); ground-based *UBV* photometry, obtained from the General Catalog of Photometric Data (GCPD) maintained at the University of Geneva (Mermilliod et al. 1997)[4]; and *JHK* photometry from the 2MASS, obtained from the 2MASS database at the NASA/IPAC Infrared Science Archive (IRSA).[5] The only processing required for these data involved the *IUE* spectrophotometry. The *IUE* data at MAST were processed by the NEWSIPS software (Nichols & Linsky 1996). As discussed in detail by Massa & Fitzpatrick (2000), these data contain significant thermal and temporal dependences and suffer from an incorrect absolute calibration. We corrected the data for their systematic errors and placed them onto the *Hubble Space Telescope* (*HST*) Faint Object Spectrograph (FOS) flux scale of Bohlin (1996) using the correction algorithms described by Massa & Fitzpatrick (2000). This step is essential for our program, since our "comparison stars" used to derive extinction curves are stellar atmosphere models, so systematic errors in the absolute calibration would not cancel as they would for Pair Method of extinction determinations.

2.3. A View of The Energy Distributions

To provide a perspective on the SEDs used to derive the extinction curves in our studies, Figure 2 shows all of the SED data for our 14 star sample. The SEDs are arbitrarily shifted vertically for display. Small circles show the *IUE* spectrophotometry in the range $\lambda \leqslant 3000$ Å, and the ACS/
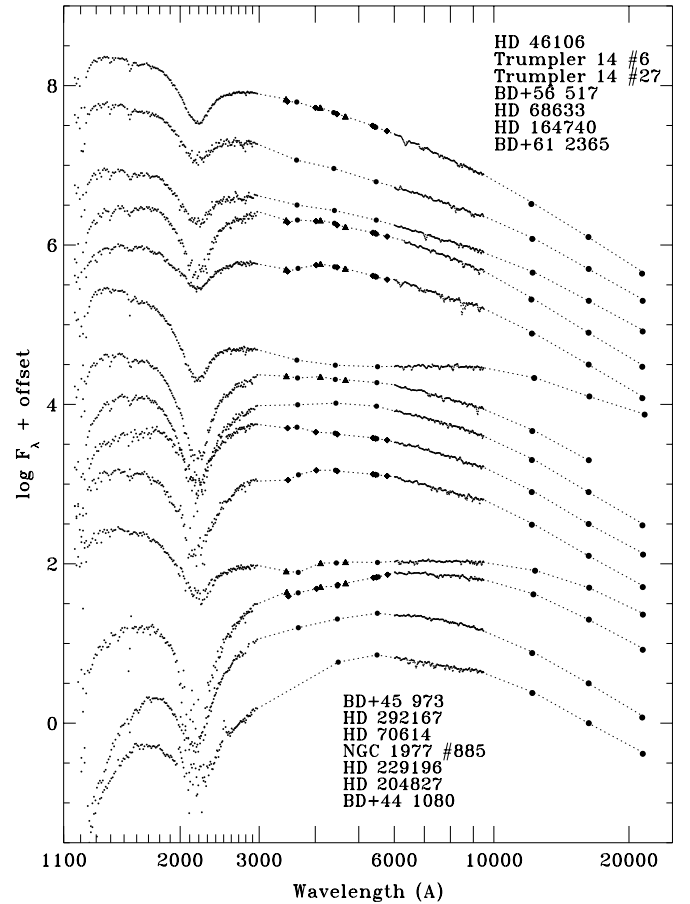

₄ The GCPD catalog was accessed at http://obswww.unige.ch/gcpd/gcpd.html.
₅ The 2MASS data were accessed at http://irsa.ipac.caltech.edu/applications/Gator.

Figure 2. Multiwavelength SEDs for the program stars. In the UV ($\lambda \leqslant 3000$ Å), low-resolution *IUE* spectrophotometry is shown as small circles. In the optical (3000 Å $< \lambda <$ 6000 Å), Johnson *UBV* Strömgren *uvby* and Geneva $UB_1B_2V_1G$ photometry are indicated by the circles, triangles, and diamonds, respectively. In the NIR, the small circles are the new ACS observations and the large circles are the 2MASS *JHK* photometry. The SEDs have been offset by arbitrary amounts for display purposes. The dashed lines are not model fits to the SEDs, but were added to guide the eye and to help distinguish the datasets for each star.

HRC/G800L data in the range 6000 Å $\leqslant \lambda \leqslant$ 9500 Å. 2MASS *JHK* values are shown as large filled circles in the NIR region ($\lambda >$ 10000 Å). In the optical, *UBV* data are indicated as filled circles. To add to the coverage, we also show ground-based Strömgren *uvby* (filled triangles) and Geneva $UB_1B_2V_1G$ (filled diamonds) photometry from the GCPD catalog whenever they are available. For all the photometry, the conversion to absolute fluxes was performed using the calibrations of Fitzpatrick & Massa (2005b). As noted above, most of the structure seen in the ACS/HRC/G800L data is instrumental. The dashed curves in the figure are shown to guide the eye and to help isolate the individual stars. These lines are not model fits.

3. THE ANALYSIS

We begin this section by creating the extinction curves that will be used in the analysis. We then test whether the NIR extinction curves can be expressed as a simple power law. We demonstrate that there is no "universal" exponent for the power law, and that the exponent which provides the best fit to a particular curve is sensitive to the wavelength range used to derive it. We also show that the $R(V)$ determined from a power-law fit to HD 164740 is inconsistent with previous estimates and with an independent estimate for $R(V)$ based on its distance and absolute magnitude. These facts destroy our confidence in

schemes which attempt to derive $R(V)$ from power-law fits, and motivate us to introduce an alternative, analytic form for NIR extinction curves. We show that this new form actually describes the NIR data as well as any power law, and that it does so over a much larger wavelength range. Further, the new formulation produces an $R(V)$ for HD 164740 which is consistent with the independent estimate. It also gives $R(V)$ values for the other program stars that agree with previous estimates.

3.1. The NIR Extinction Curves

We produced normalized NIR extinction curves, $k(\lambda - V) \equiv E(\lambda - V)/E(B - V)$ for our 14 sight lines by adopting the appropriate stellar atmosphere models derived in Paper V as the unreddened SEDs. In Paper V, the observed SEDs of 328 reddened stars—including those studied here—were fit with a combination of stellar atmospheres (to estimate the unreddened SED) and a flexible analytical representation of interstellar extinction (to model $k(\lambda - V)$, utilizing a uniform set of *IUE* UV spectrophotometry, *UBV* optical photometry, and 2MASS *JHK* NIR photometry.

For each program star here, we adopt the best-fit intrinsic SED from Paper V, which is defined by the values of $T_{\rm eff}$, $\log g$, [m/H], and $v_{\rm turb}$ listed in their Table 3. The extinction in the *JHK* bands was computed using synthetic photometry of the stellar model fluxes as described in Paper V and references therein. To mitigate noise and more clearly view trends in the ASC data, we rebinned the ACS measurements and model SEDs into 500 Å bins centered at 6250, 6750, 7250, 7750, 8250, 8750, and 9250 Å, thereby utilizing all of the ACS data within the 6000–9500 Å range of our measurements. These fluxes were then converted into seven independent magnitudes. To smooth instrumental features in the ACS data, we fitted the individual spectra with fourth-order polynomials, employing a sigma-clipping algorithm. The results were smooth representations of the ACS data, from which the synthetic magnitudes were computed. We list the values of the normalized NIR extinction for the program stars in Table 2. The labels "ACS62," "ACS67," etc. refer to the seven synthetic filters described above.

The 1σ errors listed in the table incorporate both the uncertainty in the intrinsic SEDs and the uncertainties in the ACS, *JHK*, and *V*-band measurements from which $k(\lambda - V)$ is computed. For each star, we used the 100 Monte Carlo error simulations described in Paper V, each of which yielded an independent estimate of the shape of the intrinsic SED. For each of these SEDs, we computed 20 NIR extinction curves, each using the observed photometry convolved with a random realization of the expected uncertainties in the measurements. Our noise model includes a 1σ error of ± 0.015 mag in *V* and the standard errors provided with the 2MASS *JHK* photometry. However, while calibrating synthetic photometry for use in SED modeling, we (Fitzpatrick & Massa 2005b) found that the 2MASS magnitudes—notably *H*—had a larger scatter than could be explained by the stated uncertainties. We thus quadratically combine the standard 2MASS uncertainties with values of 0.007, 0.040, and 0.017 mag for *J*, *H*, and *K*, respectively, to arrive at the total uncertainty for each magnitude. Finally, we adopted the point-to-point photometric errors produced by the aXe processing software for the ACS/HRC/G800L spectra and a 1σ zero-point uncertainty of $\pm 2.5\%$ (see the Appendix). The final result was an ensemble of 2000 curves for each star, representing the likely range of uncertainties. The errors listed in Table 2 are simply the standard deviations of each point derived from the 2000 curve set.

The data from Table 2 are plotted in Figure 3, with the key to the symbols given in the legend. Three curves are overplotted for most of the stars. These are power-law model fits which will be discussed below.

3.2. The Power-Law Model

We begin by comparing our extinction curves to a basic power-law extinction model of the form

$$A(\lambda) \propto \lambda^{-\beta}, \tag{1}$$

where $A(\lambda)$ is the total extinction at wavelength λ and β is a wavelength-independent exponent. Converting this to the normalized form of our extinction curves yields

$$k(\lambda - V) \equiv \frac{E(\lambda - V)}{E(B - V)} = k_{\rm IR}\lambda^{-\beta} - R(V), \tag{2}$$

where $k(\lambda - V)$ is a function of the power β, a scale factor $k_{\rm IR}$, and the well-known ratio of selective to total extinction $R(V)$ [$\equiv A(V)/E(B - V)$]. In the following discussion, we use nonlinear χ^2 minimization routines (Markwardt 2009) to fit the observed extinction curves with Equation (2) for two different cases. In the first, $k_{\rm IR}$ and $R(V)$ are taken as free parameters, and a "universal" value of $\beta = 1.84$ is assumed (the "β-fixed" case). In the second, $k_{\rm IR}$, β, and $R(V)$ are all allowed to vary (the "β-variable" case). Previous studies have shown that when extinction curves are modeled by Equation (1), the fits tend to diverge from observations at wavelengths shortward of the *I*-photometric band, i.e., at $\lambda \lesssim 7500$ Å (see, e.g., Figures 1–3 of Martin & Whittet 1990). Likewise, we found that, for most of our sight lines, the inclusion of ACS data shortward of 7500 Å greatly degraded the quality of the fits by increasing χ^2. Thus, we only use data with $\lambda > 7500$ Å in our power-law analyses. These data are shown in Figure 3 as large filled symbols.

The best fits to our data using Equation (2) are shown in Figure 3 as the dashed ("β-fixed") and solid ("β-variable") curves in each panel. The curves are extrapolated over the full wavelength extent of the panels, but were determined using only the data indicated by the large filled symbols. In most of the panels, it is very clear that the power-law functions fail badly for $\lambda \lesssim 7500$ Å—which led to the wavelength restriction described above. The dotted curves shown in the figures are β-variable fits to the ACS data alone, utilizing all seven of the synthetic ACS magnitudes. These curves address the ability of a specific parameterization to provide a reasonable and consistent extrapolation to longer wavelengths. This important issue will be discussed further below.

Table 3 presents the numerical results of the fits illustrated in Figure 3. The 1σ uncertainties listed in the table are determined from the ensemble of 2000 Monte Carlo noise model realizations computed for each sight line. For each parameter, they represent the dispersion of the results from power-law fits to the simulated curves about the best-fit results. The final column of Table 3 gives the *F*-statistic, constructed from the χ^2 values for the β-fixed and β-variable cases. The *F*-statistic can be used to determine whether the addition of a new fitting term (in this case β) significantly improves the fit. Large *F* values, i.e., $F \gtrsim 10$, indicate the validity of the new parameter, while progressively smaller *F* values indicate progressively less justification (see, e.g., Bevington 1969). Although to the eye most of the fits in Figure 3 look reasonable, the *F*-statistic demonstrates that the fits for at least half of the sight lines are significantly improved

Table 2
NIR Extinction Curves for Target Stars

Star	k(λ-V)									
	K (2.18 μm)	H (1.62 μm)	J (1.23 μm)	ACS92 (9250 Å)	ACS87 (8750 Å)	ACS82 (8250 Å)	ACS77 (7750 Å)	ACS72 (7250 Å)	ACS67 (6750 Å)	ACS62 (6250 Å)
BD+56 517	−2.79 ± 0.09	−2.65 ± 0.12	−2.34 ± 0.08	−1.95 ± 0.08	−1.81 ± 0.08	−1.65 ± 0.07	−1.43 ± 0.07	−1.18 ± 0.07	−0.92 ± 0.07	−0.70 ± 0.07
BD+45 973	−2.47 ± 0.05	−2.33 ± 0.08	−2.07 ± 0.04	−1.58 ± 0.05	−1.46 ± 0.05	−1.31 ± 0.05	−1.13 ± 0.05	−0.92 ± 0.04	−0.69 ± 0.04	−0.44 ± 0.04
BD+44 1080	−2.15 ± 0.04	−2.01 ± 0.06	−1.80 ± 0.04	−1.38 ± 0.04	−1.26 ± 0.04	−1.12 ± 0.04	−0.94 ± 0.04	−0.77 ± 0.04	−0.60 ± 0.04	−0.37 ± 0.03
NGC 1977 #885	−4.58 ± 0.08	−4.24 ± 0.10	−3.47 ± 0.06	−2.43 ± 0.06	−2.21 ± 0.05	−1.96 ± 0.05	−1.67 ± 0.05	−1.36 ± 0.05	−1.02 ± 0.04	−0.63 ± 0.04
HD 46106	−2.56 ± 0.10	−2.54 ± 0.14	−2.16 ± 0.09	−1.64 ± 0.09	−1.47 ± 0.09	−1.31 ± 0.09	−1.16 ± 0.08	−0.96 ± 0.08	−0.76 ± 0.08	−0.52 ± 0.08
HD 292167	−2.87 ± 0.06	−2.59 ± 0.09	−2.31 ± 0.05	−1.78 ± 0.05	−1.59 ± 0.05	−1.43 ± 0.05	−1.26 ± 0.05	−1.05 ± 0.05	−0.82 ± 0.05	−0.53 ± 0.05
HD 68633	−3.31 ± 0.10	−3.18 ± 0.14	−2.76 ± 0.08	−2.17 ± 0.08	−2.00 ± 0.08	−1.75 ± 0.08	−1.49 ± 0.08	−1.27 ± 0.07	−1.06 ± 0.07	−0.73 ± 0.07
HD 70614	−2.85 ± 0.07	−2.64 ± 0.12	−2.34 ± 0.06	−1.84 ± 0.06	−1.67 ± 0.06	−1.49 ± 0.06	−1.27 ± 0.05	−1.04 ± 0.05	−0.82 ± 0.05	−0.56 ± 0.05
Trumpler 14 #6	−4.18 ± 0.12	−3.85 ± 0.14	−3.27 ± 0.10	−2.32 ± 0.09	−2.12 ± 0.09	−1.88 ± 0.08	−1.62 ± 0.08	−1.36 ± 0.08	−1.05 ± 0.07	−0.63 ± 0.07
Trumpler 14 #27	−3.76 ± 0.10	−3.43 ± 0.12	−2.87 ± 0.08	−2.05 ± 0.07	−1.87 ± 0.07	−1.62 ± 0.07	−1.36 ± 0.06	−1.11 ± 0.06	−0.85 ± 0.06	−0.53 ± 0.06
HD 164740	−4.92 ± 0.08	−4.22 ± 0.09	−3.49 ± 0.06	−2.48 ± 0.05	−2.22 ± 0.05	−1.95 ± 0.05	−1.67 ± 0.05	−1.36 ± 0.04	−1.04 ± 0.04	−0.65 ± 0.04
HD 229196	−2.88 ± 0.04	−2.69 ± 0.05	−2.34 ± 0.03	−1.74 ± 0.03	−1.59 ± 0.03	−1.42 ± 0.03	−1.24 ± 0.03	−1.04 ± 0.03	−0.82 ± 0.03	−0.56 ± 0.03
HD 204827	−2.25 ± 0.04	−2.17 ± 0.05	−1.92 ± 0.03	−1.51 ± 0.04	−1.40 ± 0.04	−1.26 ± 0.04	−1.10 ± 0.03	−0.92 ± 0.03	−0.71 ± 0.03	−0.43 ± 0.03
BD+61 2365	⋯	−2.68 ± 0.07	−2.30 ± 0.05	−1.74 ± 0.05	−1.59 ± 0.05	−1.41 ± 0.05	−1.21 ± 0.05	−1.00 ± 0.05	−0.77 ± 0.04	−0.50 ± 0.04

Table 3
Results for Power-Law Fits

Star	β-Fixed[a]				β-Variable[b]				F[c]
	k_{IR}	β	$R(V)$	χ^2	k_{IR}	β	$R(V)$	χ^2	
BD+56 517	$0.98^{+0.06}_{-0.04}$	1.84	$3.03^{+0.07}_{-0.07}$	0.17	$0.87^{+0.15}_{-0.10}$	$2.10^{+0.18}_{-0.29}$	$2.95^{+0.13}_{-0.07}$	0.16	1.1
BD+45 973	$1.00^{+0.04}_{-0.02}$	1.84	$2.73^{+0.04}_{-0.03}$	0.07	$0.93^{+0.06}_{-0.06}$	$2.00^{+0.15}_{-0.11}$	$2.68^{+0.06}_{-0.06}$	0.03	8.8
BD+44 1080	$0.89^{+0.03}_{-0.02}$	1.84	$2.39^{+0.04}_{-0.03}$	0.29	$0.76^{+0.05}_{-0.04}$	$2.21^{+0.15}_{-0.12}$	$2.28^{+0.04}_{-0.04}$	0.02	63.6
NGC 1977 #885	$2.13^{+0.04}_{-0.04}$	1.84	$4.99^{+0.05}_{-0.07}$	2.40	$2.97^{+0.18}_{-0.09}$	$1.26^{+0.04}_{-0.08}$	$5.74^{+0.17}_{-0.10}$	0.64	14.9
HD 46106	$1.09^{+0.07}_{-0.05}$	1.84	$2.88^{+0.09}_{-0.07}$	0.23	$1.00^{+0.15}_{-0.10}$	$2.03^{+0.30}_{-0.20}$	$2.81^{+0.17}_{-0.10}$	0.26	0.4
HD 292167	$1.18^{+0.03}_{-0.04}$	1.84	$3.12^{+0.04}_{-0.05}$	0.24	$1.28^{+0.10}_{-0.08}$	$1.66^{+0.10}_{-0.13}$	$3.21^{+0.09}_{-0.08}$	0.22	1.4
HD 68633	$1.35^{+0.06}_{-0.04}$	1.84	$3.69^{+0.08}_{-0.07}$	0.24	$1.14^{+0.10}_{-0.09}$	$2.24^{+0.19}_{-0.16}$	$3.52^{+0.10}_{-0.10}$	0.11	6.5
HD 70614	$1.15^{+0.04}_{-0.03}$	1.84	$3.13^{+0.06}_{-0.05}$	0.13	$1.06^{+0.09}_{-0.07}$	$2.02^{+0.14}_{-0.21}$	$3.06^{+0.09}_{-0.07}$	0.12	1.8
Trumpler 14 #6	$1.90^{+0.08}_{-0.05}$	1.84	$4.58^{+0.12}_{-0.07}$	0.34	$2.34^{+0.20}_{-0.17}$	$1.44^{+0.10}_{-0.11}$	$4.98^{+0.20}_{-0.12}$	0.12	10.7
Trumpler 14 #27	$1.75^{+0.06}_{-0.04}$	1.84	$4.12^{+0.08}_{-0.06}$	0.35	$2.16^{+0.21}_{-0.11}$	$1.45^{+0.09}_{-0.13}$	$4.48^{+0.20}_{-0.11}$	0.03	53.7
HD 164740	$2.26^{+0.04}_{-0.04}$	1.84	$5.17^{+0.06}_{-0.06}$	5.51	$4.27^{+0.39}_{-0.24}$	$0.89^{+0.04}_{-0.06}$	$7.04^{+0.38}_{-0.25}$	0.10	283.1
HD 229196	$1.23^{+0.02}_{-0.02}$	1.84	$3.17^{+0.03}_{-0.03}$	0.42	$1.29^{+0.04}_{-0.04}$	$1.72^{+0.07}_{-0.06}$	$3.23^{+0.04}_{-0.05}$	0.43	1.0
HD 204827	$0.86^{+0.03}_{-0.02}$	1.84	$2.49^{+0.04}_{-0.02}$	0.46	$0.73^{+0.04}_{-0.04}$	$2.24^{+0.13}_{-0.10}$	$2.38^{+0.04}_{-0.03}$	0.11	16.5
BD+61 2365	$1.21^{+0.05}_{-0.03}$	1.84	$3.14^{+0.05}_{-0.05}$	0.09	$1.38^{+0.34}_{-0.17}$	$1.61^{+0.28}_{-0.34}$	$3.30^{+0.32}_{-0.16}$	0.05	3.7

Notes.

[a] "Universal" value of $\beta = 1.84$ assumed in these fits. Reduced-χ^2 values are shown, corresponding to 5 degrees of freedom. Fits for the sight line toward BD+61 2365, for which no K-band data are available, have 4 degrees of freedom.

[b] Power-law exponent β taken as a free parameter in these fits. Reduced-χ^2 values are shown, corresponding to 4 degrees of freedom. Fits for the sight line toward BD+61 2365 have 3 degrees of freedom.

[c] The F-statistic, which tests the need to include β as a free parameter in the power-law fits (Bevington 1969).

by allowing a variable β, strongly justifying the inclusion of β as a free parameter. The largest F values tend to occur for the sight lines whose $R(V)$ values differ most from the Galactic mean of 3.1, particularly those with the largest $R(V)$. The inability of the $\beta = 1.84$ model to adequately represent large $R(V)$ sight lines is readily apparent in the last panel of Figure 3.

An essentially identical method of assessing the statistical significance of the derived β values is simply to compare them with the "universal" value of 1.84. If the new values differ from 1.84 by 2σ or more—which is the case for seven of our sight lines—then there is very strong statistical justification for rejecting 1.84 as the appropriate value of β. A visual illustration of the significance of the derived β's is shown in the top panel of Figure 4, where we plot β from the β-variable case against $E(B - V)$ for each sight line. The dotted line is $\beta = 1.84$. The sample mean and median values of β are 1.78 and 2.00, respectively. These are not far from the universal value, although the figure clearly illustrates significant departures exist. The figure also demonstrates that 1.84 cannot be replaced by some better-determined universal value. Indeed, it challenges the notion of the existence of a universal IR extinction law.

A further challenge to the universal extinction model is shown in the lower panel of Figure 4, where we plot β against $R(V)$ for each sight line. Note that these $R(V)$ values are determined by extrapolating the power-law models to $\lambda^{-1} = 0$—a practice which will be discussed further below. As might be anticipated from Equation (2), the uncertainties in β and $R(V)$ are correlated, and the directions and strengths of the correlations are indicated in the figure by the 1σ error bars. For comparison, we also show the values of β and $R(V)$ for the star ρ Oph from Martin & Whittet (1990; filled triangle). The consistency of the power-law exponent for this dense cloud sight line with the results for diffuse cloud sight lines has been a significant motivation for the perception of a universal $\beta \simeq 1.8$ law (e.g., Figure 3.7 in Whittet 2003). Although the ρ Oph measurements were not made in the same manner as ours, they utilize data over the same wavelength range (I through K band) and should be compatible. The data in Figure 4 reveal a striking

systematic trend—β is anti-correlated with $R(V)$ in the sense that large-$R(V)$ sight lines have smaller than average values of β. As $R(V)$ is generally considered a coarse indicator of grain size, i.e., populations of larger-than-average grains yield larger-than-average $R(V)$ (e.g., see Mathis & Wallenhorst 1981), our results indicate that the shape of IR extinction curves parameterized by β are environmentally dependent. As shown in Paper V, there is considerable intrinsic scatter in correlations between $R(V)$ and other properties of interstellar extinction curves, and often the correlations are only apparent when the most extreme $R(V)$ values are considered. Our results suggest that previous analyses have not had access to a wide-enough range in $R(V)$ to reveal the environmental dependence of β.

Since a major motivation for using an analytic form for extinction is to extrapolate the curve to infinite wavelength and estimate $R(V)$, it is troubling that the $R(V)$s derived from the power-law curves depend strongly on the adopted exponent. Figure 3 and Table 3 show that the β-fixed and β-variable approaches give similar results when $R(V)$ is near the Galactic mean of $\sim$3.1, but yield increasingly divergent results at both larger and smaller $R(V)$. This is best illustrated by the HD 164740 sight line. This is the most extreme sight line in our sample in the sense that it has the smallest β and largest $R(V)$. Furthermore, there is no indication that it is pathological, since Figure 4 shows that it is consistent with an extrapolation of the trends exhibited by less extreme sight lines. The problem with HD 164740 is that, even though the β-variable fit provides a fine representation for the I through K-band extinction (see Figure 3), the extrapolation of its power-law fit to longer wavelengths is inconsistent with the physical expectation that $\frac{dk(\lambda-V)}{d\lambda} \to 0$ as $\lambda \to \infty$, (which demands $\beta \geqslant 1$).

An additional, but related, problem is that the $R(V)$ determined from the β-variable fit for HD 164740 is demonstrably incorrect. HD 164740 is a member of the cluster NGC 6530, whose distance, d, has been determined independently of HD 164740. Therefore, given its absolute magnitude, M_V, it is possible to derive an independent estimate for $R(V)$ by rearranging the formula for the distance modulus.
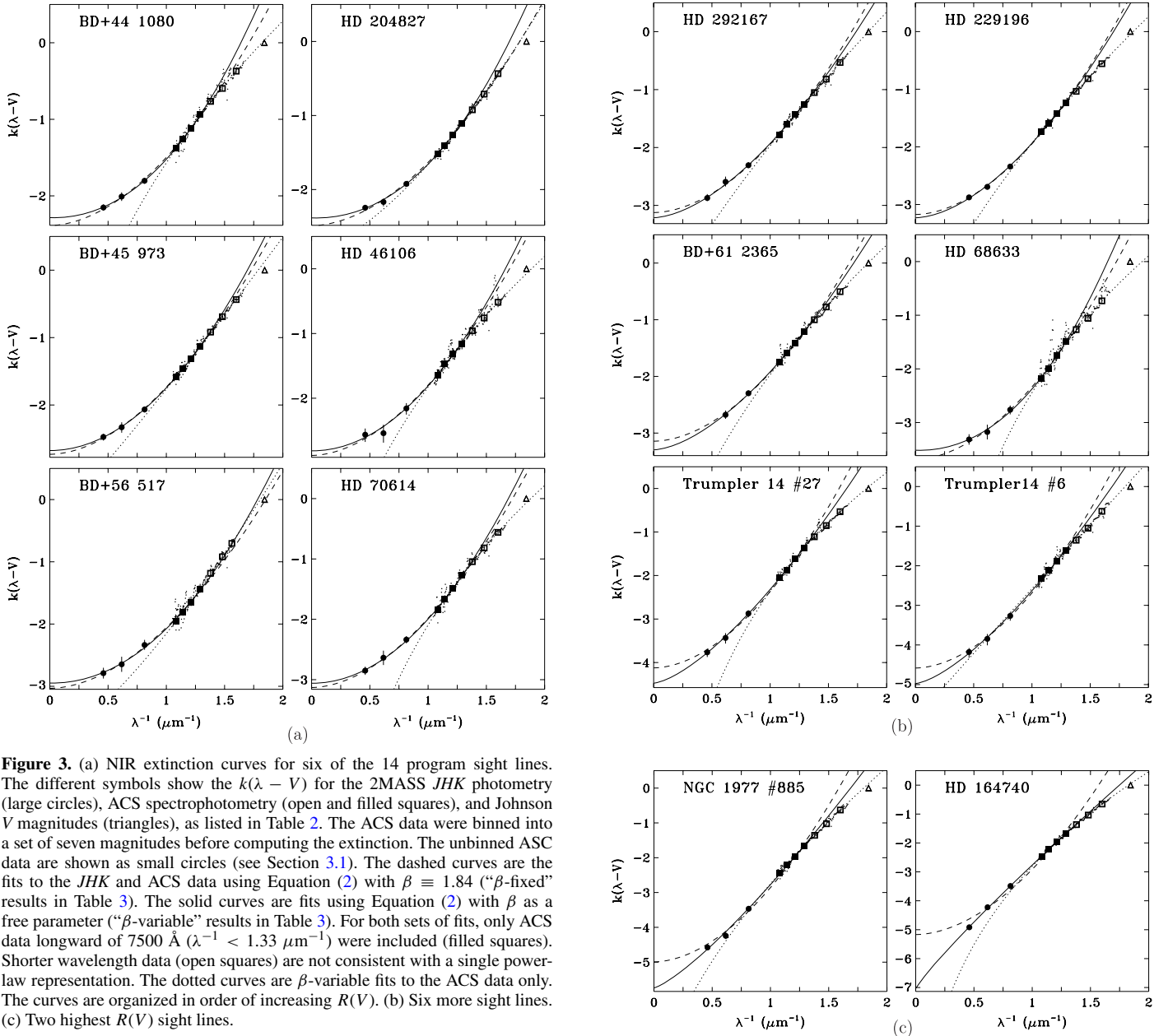
Figure 3. (a) NIR extinction curves for six of the 14 program sight lines. The different symbols show the $k(\lambda - V)$ for the 2MASS *JHK* photometry (large circles), ACS spectrophotometry (open and filled squares), and Johnson *V* magnitudes (triangles), as listed in Table 2. The ACS data were binned into a set of seven magnitudes before computing the extinction. The unbinned ASC data are shown as small circles (see Section 3.1). The dashed curves are the fits to the *JHK* and ACS data using Equation (2) with $\beta \equiv 1.84$ ("β-fixed" results in Table 3). The solid curves are fits using Equation (2) with β as a free parameter ("β-variable" results in Table 3). For both sets of fits, only ACS data longward of 7500 Å ($\lambda^{-1} < 1.33$ μm^{-1}) were included (filled squares). Shorter wavelength data (open squares) are not consistent with a single power-law representation. The dotted curves are β-variable fits to the ACS data only. The curves are organized in order of increasing $R(V)$. (b) Six more sight lines. (c) Two highest $R(V)$ sight lines.

Figure 3. (Continued)

Specifically,

$$R(V) = \frac{V - M_V - 5\log(d/10pc)}{E(B - V)}. \qquad (3)$$

The data needed to compute $R(V)$ for HD 164740 are d = 1330 pc (Paper V), $M_V = -4.8$ (Walborn 1973), $V =$ 10.30 mag and $E(B - V) = 0.86$ (see Table 1). We consider two cases which span the range of expected absolute magnitudes: a single star or a binary with identical components. Using these data for HD 164740, we find $5.2 \leqslant R(V) \leqslant 6.1$. These values are significantly smaller than the $R(V) = 7.0$ inferred from extrapolation of the β-variable power-law fit. One can appeal to uncertainties in the distance and absolute magnitude of HD 164740, but these are insufficient to explain such a large discrepancy. In support of this conclusion, Hecht et al. (1982) find $R(V) = 5.6$ based on a comparison of the brightness and color of HD 164740 with those of the nearby—and presumably equally distant—O-type star HD 164794 (9 Sgr). Note that other

estimates of $R(V)$ for HD 164740 have been made by extrapolating an assumed form for NIR extinction by, for example, Cardelli et al. (1989) $[R(V) = 5.30]$ and more recently by us in Paper V $[R(V) = 5.21]$. However, the assumed forms, which are (or resemble) power laws with large exponents ($\beta =1.6$–1.84) are clearly inconsistent with the observed shape of the NIR extinction curve of HD 164740. Thus, these results cannot be used to prove an error in the β-variable value.

The HD 164740 discussion shows that, even though a power law can fit an NIR extinction curve quite well over a specific wavelength interval, extrapolation of such fits to longer wavelengths can be unreliable. This was anticipated by Martin & Whittet (1990) who noted that it would be "remarkable" for a single power law to be appropriate over an extended wavelength range. Nevertheless, this caveat is explicitly ignored when a single-exponent power law is used to estimate $R(V)$. To emphasize this point, consider the dotted curves in Figure 3.
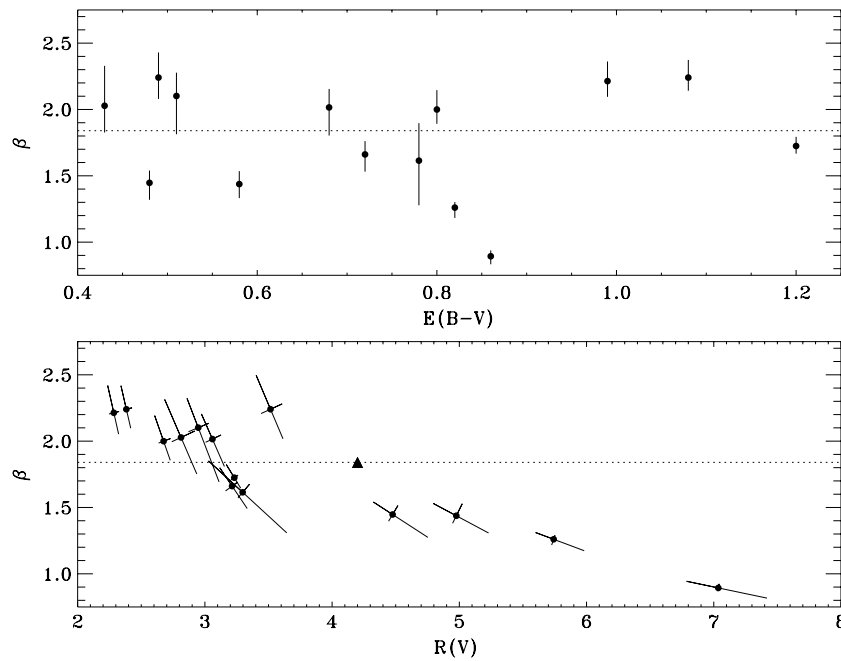
Figure 4. Power-law exponent β vs. $E(B-V)$ (top panel) and $R(V)$ (bottom panel) for the "β-variable" fits from Table 3. The dotted horizontal lines show the value $\beta = 1.84$. The filled triangle in the lower panel represents the sight line to the star ρ Oph from Martin & Whittet (1990). The 1σ error bars are based on fits to the Monte Carlo simulations of the data and the noise model.

These are power-law fits (Equation (2)) to all of the ACS data, i.e., covering the full 6000–9500 Å wavelength range. While they certainly provide an excellent analytical representation of $k(\lambda - V)$ at these wavelengths ($\chi^2 < 0.2$ and, in 12-of-14 cases, $\chi^2 < 0.1$), nevertheless it is quite clear that extrapolations of these fits to longer wavelengths are grossly inconsistent with the *JHK* data and, consequently, the intercepts of the extrapolated curves are totally unrelated to $R(V)$. In addition, the βs are always smaller than those inferred from the *I*-band through *K*-band fits in Table 3 and are nearly always less than the limiting value of 1. These results suggest a systematic effect in which the exponent of a best-fit power-law systematically decreases as shorter wavelengths are considered and the implied $R(V)$ increases.

At this point, several straightforward conclusions can be drawn.

1. All of our NIR extinction curves can indeed be well represented by a simple power-law formulation in the *I*-band through *K*-band spectral region.
2. However, the power-law exponent, β, varies significantly from sight line-to-sight line, and is incompatible with the thesis of a universal form to NIR extinction.
3. The value of the exponent, β, is anti-correlated with $R(V)$, suggesting that the detailed shape of NIR extinction curves is likely a function of the line-of-sight grain size distribution.
4. The parameters of power-law fits can depend quite strongly on the wavelength interval used to determine them, with the value of β tending to decrease as shorter wavelengths are included. This result implies that extrapolations of power-law fits to longer wavelengths can be an unreliable means for estimating $R(V)$.

3.3. An Alternative Model

Given the problems encountered with the simple power-law representation for NIR extinction, we decided to search

for a different functional form, whose parameters can be estimated from accessible data and can be extrapolated to long wavelengths to obtain consistent, meaningful estimates of $R(V)$. While many such forms are possible, the one introduced by Pei (1992) in a study of Milky Way and Magellanic Cloud extinction produced remarkably good results.[6] We use a generalized version of the function, with more degrees of freedom. It has the form

$$k(\lambda - V) = k_{IR} \frac{1}{1 + (\lambda/\lambda_0)^\alpha} - R(V), \quad (4)$$

where α, k_{IR}, λ_0, and $R(V)$ are potentially free parameters. For $\lambda \gg \lambda_0$, this function reduces to a power law with exponent $-\alpha$. For $\lambda \ll \lambda_0$, it flattens to a constant whose value is $k_{IR} - R(V)$. Between these extremes, it resembles power law whose exponent increases with wavelength—which is exactly the behavior suggested by our analysis in the previous section.

While the introduction of four free parameters may seem a steep price to pay for abandoning the simpler power-law formulation, we quickly discovered that two strong observational constraints can be placed on the parameters. The first is that λ_0 can be replaced by constant for all of our sight lines, which span a wide range of extinction properties, without significant loss of accuracy. The second is that the scale factor, k_{IR}, can be expressed as a linear function of $R(V)$, again without loss of accuracy. These constraints result in a simplified version of Equation (4) given by

$$k(\lambda - V) = [0.349 + 2.087 R(V)] \frac{1}{1 + (\lambda/0.507)^\alpha} - R(V), \quad (5)$$

where λ is in μm. Equation (5) contains only two free parameters, α and $R(V)$; the same number as the β-fixed power-law model, and one less than the β-variable model.

---

[6] We thank Karl Gordon for bringing this form to our attention. It was used in a study of Galactic extinction curves by Clayton et al. (2003) and a more general discussion of its utility will be given in K. Gordon (2009, in preparation).
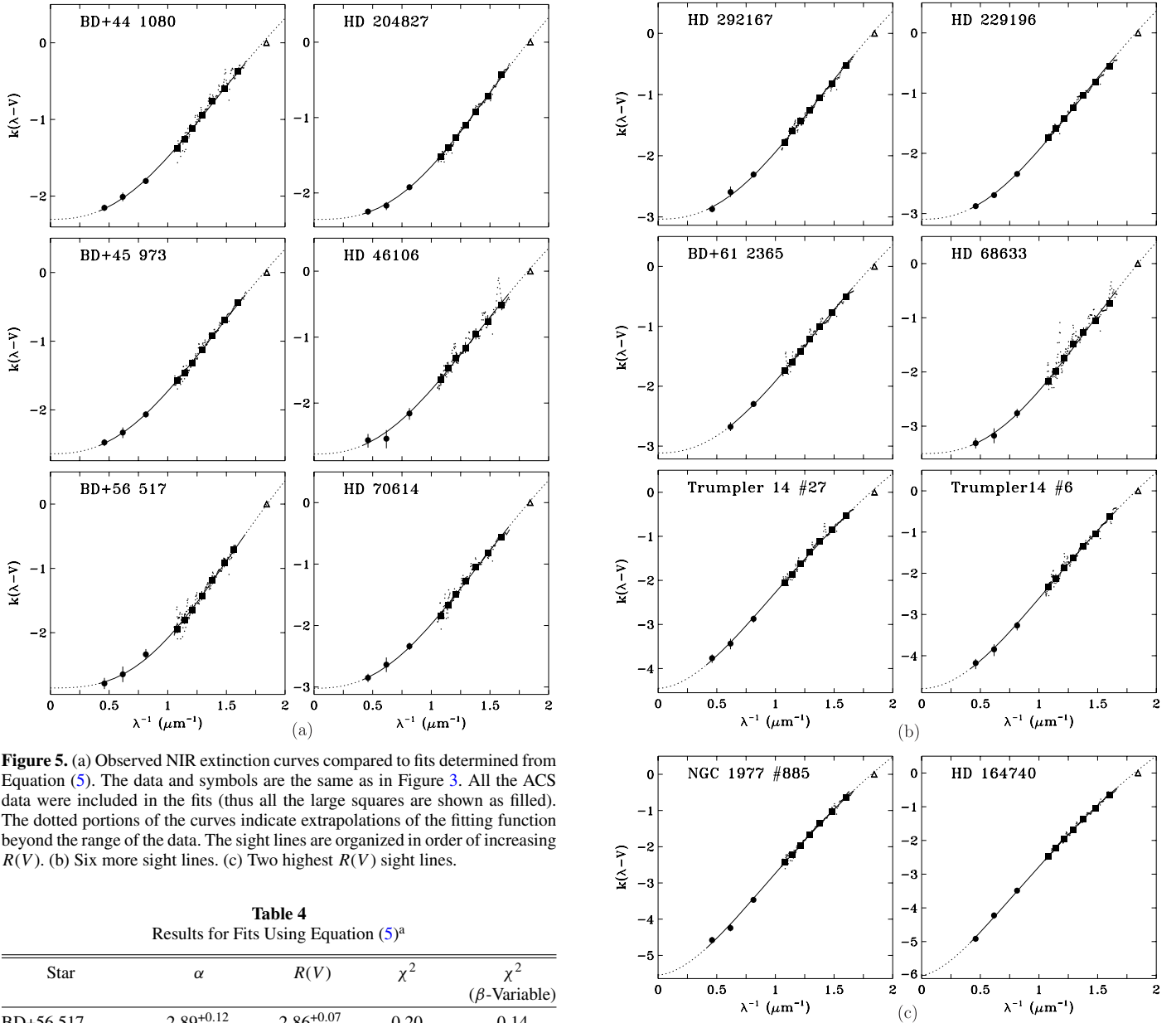
Figure 5. (a) Observed NIR extinction curves compared to fits determined from Equation (5). The data and symbols are the same as in Figure 3. All the ACS data were included in the fits (thus all the large squares are shown as filled). The dotted portions of the curves indicate extrapolations of the fitting function beyond the range of the data. The sight lines are organized in order of increasing $R(V)$. (b) Six more sight lines. (c) Two highest $R(V)$ sight lines.

Table 4
Results for Fits Using Equation (5)[a]

Star	α	$R(V)$	χ^2	χ^2 (β-Variable)
BD+56 517	$2.89^{+0.12}_{-0.15}$	$2.86^{+0.07}_{-0.07}$	0.20	0.14
BD+45 973	$2.49^{+0.08}_{-0.10}$	$2.64^{+0.06}_{-0.04}$	0.13	0.23
BD+44 1080	$2.47^{+0.06}_{-0.10}$	$2.30^{+0.05}_{-0.03}$	0.30	0.69
NGC 1977 #885	$1.73^{+0.05}_{-0.06}$	$5.54^{+0.12}_{-0.11}$	0.38	0.87
HD 46106	$2.45^{+0.20}_{-0.25}$	$2.77^{+0.12}_{-0.08}$	0.17	0.33
HD 292167	$2.40^{+0.10}_{-0.09}$	$3.04^{+0.06}_{-0.07}$	0.21	0.22
HD 68633	$2.54^{+0.09}_{-0.15}$	$3.51^{+0.11}_{-0.08}$	0.38	0.60
HD 70614	$2.48^{+0.09}_{-0.10}$	$3.02^{+0.07}_{-0.06}$	0.22	0.48
Trumpler 14 #6	$1.94^{+0.08}_{-0.11}$	$4.80^{+0.21}_{-0.16}$	0.10	0.24
Trumpler 14 #27	$1.81^{+0.08}_{-0.10}$	$4.45^{+0.19}_{-0.11}$	0.18	0.43
HD 164740	$1.61^{+0.04}_{-0.05}$	$6.00^{+0.15}_{-0.12}$	0.15	0.20
HD 229196	$2.34^{+0.05}_{-0.05}$	$3.09^{+0.04}_{-0.04}$	0.75	1.27
HD 204827	$2.75^{+0.07}_{-0.09}$	$2.35^{+0.04}_{-0.02}$	0.13	0.24
BD+61 2365	$2.28^{+0.11}_{-0.12}$	$3.11^{+0.11}_{-0.09}$	0.08	0.19

Note.
[a] The final column is χ^2 for fits using the β-variable model applied to the same wavelength range used in the fits employing Equation (5).

Equation (5) proved so successful in reproducing the shapes of the NIR extinction curves that we applied it to the *JHK* data and the entire wavelength range of the ACS data. The results are

Figure 5. (Continued)

given in Table 4 and Figures 5 and 6. In Figure 5, the solid portion of the curves indicate the wavelength interval over which the fit was performed, and the dotted portions show extrapolations of the fit to longer and shorter wavelengths. Note that, although the *V*-band point was not included in the fits, extrapolations of them pass quite close to it. In fact, the *V* band could have been included in the fits without much loss of overall accuracy. Table 4 gives the α and $R(V)$ that result from the fits and their uncertainties. These are plotted in Figure 6. The correlated uncertainties were computed as described in Section 3.2. The range in α and the relationship between α and $R(V)$ mimic those of the β-variable fits discussed in Section 3.2.

That Equation (5) provides a much better fit to the observed NIR extinction curves can be seen by comparing the mean χ^2 values listed in Tables 3 and 4 for the different models. The mean χ^2 values for the β-fixed, and Equation (5) are 0.78 and 0.24, respectively. Thus, even though the fits using Equation (5) include more points, their mean χ^2 is much better than the two-parameter β-fixed power-law model. Furthermore,
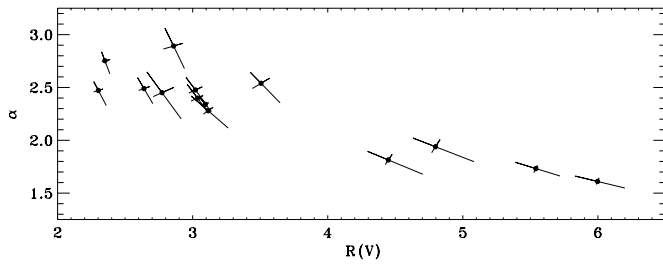
Figure 6. Plot of the α and $R(V)$ from Table 4. The 1σ error bars are based on fits to the Monte Carlo simulations of the data and the noise model.

unlike the β-fixed model, Equation (5) provides a good fit for *all* of the curves.

Notice that although the mean χ^2 for the three-parameter β-variable from Table 3 is slightly better than the Equation (5) value (0.17 compared to 0.24), a fairer comparison between the two is given in Table 4. The last column of the table lists the χ^2 values that result from fitting β-variable models to the same data as the Equation (5) fits. In this case, we see that the mean χ^2 for the β-variable fits is 0.44, considerably larger than the 0.24 that results from the Equation (5) fits.

An additional advantage to the formulation in Equation (5) is its robustness to changes in the wavelength coverage of the data. For instance, if we fit only the ACS data, spanning the wavelength range 6000–9500 Å, then the resultant values of $R(V)$ differ on average by only +0.09 from the results in Table 4, with a mean scatter of ± 0.27 and no systematic trends. Likewise the implied α values differ on average from those in Table 4 by -0.05, with a scatter of ± 0.20. Thus, in striking contrast to the β-variable case, a reliable and stable estimate of IR extinction can be derived, even in the absence of longer wavelength *JHK* data.

It is important to determine whether the values of $R(V)$ determined by Equation (5) agree with previous estimates. To begin, we note that the $R(V)$ value determined for HD 164740 is 6.00, within the expected range described in Section 3.2. We can also make a broader comparison by comparing the values in Table 5 to a commonly used means to estimate $R(V)$, which is based on optical and *JHK* photometry. This approach estimates $R(V)$ from the relation $R(V) = -1.1 \frac{E(K-V)}{E(B-V)}$, which is based on van de Hulst's theoretical extinction curve No. 15 (e.g., Johnson 1968). While, in general, our results show that two parameters are needed to fully define an NIR extinction curve, this does not exclude the possibility that relationships may exist between specific properties of the curves, at least to a high degree of approximation. Figure 7 is a plot of $\frac{E(K-V)}{E(B-V)}$ (Table 2) versus $R(V)$ from Table 4. The two quantities are clearly strongly correlated. The van de Hulst-based formula (dashed line) follows the general trend for low and moderate values of $R(V)$, but systematically underestimates it for large-$R(V)$ sight lines. Nevertheless, the overall agreement is quite good, with an rms deviation of 0.26 in $R(V)$, implying that the $R(V)$ values determined by Equation (5) are in general agreement with previous estimates.

In fact, if we assume that the $R(V)$ derived from Equation (5) are correct, we can derive a more accurate means for determining $R(V)$ from the broadband photometry. The solid line in Figure 7 is the unweighted linear fit, $R(V) = -1.36 \frac{E(K-V)}{E(B-V)} - 0.79$, which has an rms deviation for $R(V)$ of 0.13. Note that both lines yield similar results for $R(V) \lesssim 3.5$.

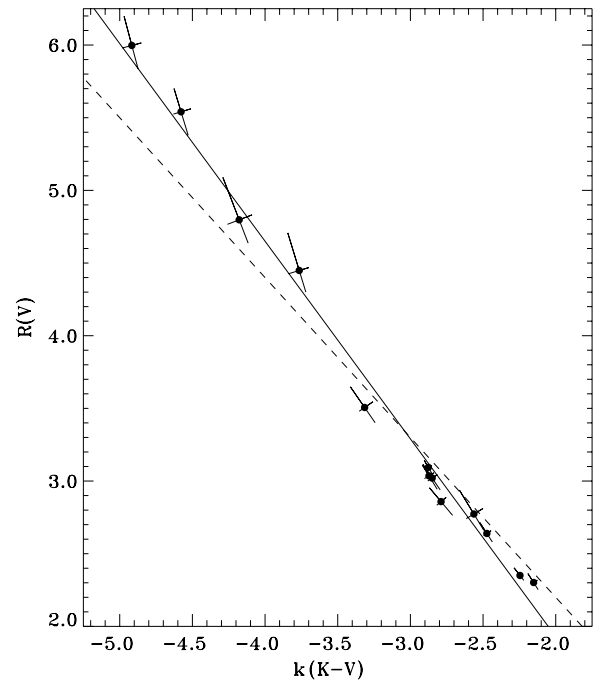The major conclusions from this section are as follows.

Figure 7. Plot of the observed $k(K-V) \equiv E(K-V)/E(B-V)$ vs. the $R(V)$ derived from fits to Equation (5). The 1σ error bars illustrate the correlated errors in the two quantities. The dashed line gives the often-used relation $R(V) = -1.1 \frac{E(K-V)}{E(B-V)}$, which is based on van de Hulst's theoretical extinction curve No. 15 (see, e.g., Johnson 1968). An unweighted least squares linear fit to the data is shown as the solid line, $R(V) = -1.36 \frac{E(K-V)}{E(B-V)} - 0.79$.

1. Equation (4) mimics a power law whose exponent increases with wavelength, which is exactly the behavior our analysis in Section 3.2 implied was needed.
2. Initial fits to the data demonstrated that the number of free parameters needed to fit NIR curves can be reduced to 2 (see, Equation (5)).
3. Equation (5) provides good fits to all of the extinction curves, and even performs better than the β-variable model, which has one more free parameter.
4. Equation (5) produces $R(V)$ values which are consistent with independent estimates, and are in accord with commonly used methods for estimating $R(V)$.
5. Equation (5) gives $R(V)$ values that do not depend strongly or systematically on the wavelength interval used to derive them.
6. For our data, the relation $R(V) = -1.36 \frac{E(K-V)}{E(B-V)} - 0.79$ reproduces $R(V)$ to within ± 0.12 over a large range in $R(V)$.

4. DISCUSSION

In general, there are two motivations for determining an analytical model for the shapes of interstellar extinction curves. The first is that it allows a consistent interpolation or extrapolation of extinction properties into spectral regions where measurements are lacking. This is used to define $R(V)$ and, hence, $A(V)$. The second is that the functional dependence of extinction over some particular spectral region may shed light on the physical processes controlling the extinction, e.g., the composition and size distribution of the grains responsible for the extinction. Further, the analytic representation may yield specific parameters whose range of variability could be related to how the grain populations respond to different physical environments along the line
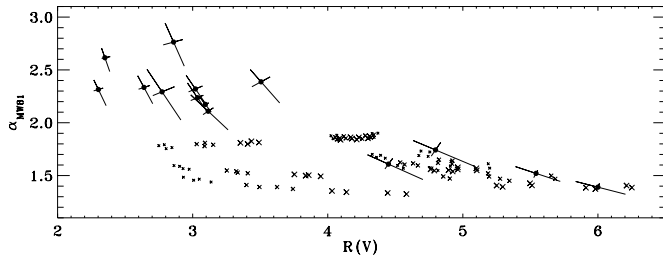
Figure 8. Comparison of extinction curve parameters derived from observed and theoretical extinction curves. α_{MW81} is the exponent that results from a simple power-law fit (see Equation (2)) to the IR extinction at $\lambda^{-1} = 0.00$, 0.29, and 1.11 μm^{-1}. It provides a measure of the shape of the curves for $\lambda > 9000$ Å. The crosses show α_{MW81} and $R(V)$ calculated from the Mathis & Wallenhorst (1981) theoretical extinction curves for a variety of size distributions and abundance ratios (see text). The small, medium, and large crosses correspond to $(C/Si)_{dust}$ = 3.25, 6.5, and 13.0, respectively. The filled circles show the same quantities derived from the best-fitting NIR curves shown in Figure 5. This figure shows that some combinations of model dust abundance and size distribution are not favored by nature. Most notable, are the crosses in the lower left of the figure, which does not contain observed points. The models in this region correspond to size distributions with small upper cutoffs for silicates ($a_+ = 0.25$ μm) and large upper cutoffs for graphite ($a_+ = 0.40$ or 0.50 μm). The Mathis & Wallenhorst (1981) models are not useful for addressing the shapes of the smaller $R(V)$ sight lines.

of sight. The first of these goals was addressed in the previous section. Here, we focus on the second.

Our results suggest that at least two parameters are needed to characterize the NIR extinction, $R(V)$ and α. It seems reasonable to suggest that $R(V)$ provides a measure of the mean grain size along the line of sight, and that α is probably related to the grain size distribution. This is because, in the small particle limit (where the ratio of grain-size to wavelength is small—as in the IR), Mie scattering theory implies that both absorption and scattering are expected to approach power-law forms with an exponent of 4 for scattering and $\sim$1 for absorption (see Chapter 7 of Spitzer 1978). Power-law exponents determined in the NIR generally lie between these two extremes. Given the sensitivity of extinction to grain properties, however, it would be surprising for extinction to adhere strictly to a single-exponent power-law form over an extended wavelength range (Martin & Whittet 1990).

In fact, these arguments make the suggestion of a universal power-law exponent for the IR troubling. It is clear from the study of other aspects of extinction (e.g., the shape of UV extinction curves) that the properties of grain populations differ significantly from place to place in interstellar space. As Martin & Whittet (1990) note, since the absorption and scattering properties of grains are generally strongly dependent on the grain composition and size, the suggestion of universality requires highly constrained sight line-to-sight line modifications in grain properties which must occur in such a way as to yield, for example, a range in $R(V)$ but a single IR power-law exponent. Our results remove this troubling constraint. We find that the exponent is spatially variable and likely does reflect underlying differences in the grain populations.

To verify that the observational parameters obtained from Equation (5) are consistent with grain models and to determine whether they can be used to constrain the grain parameters, we compare our results with the theoretical calculations given by Mathis & Wallenhorst (1981, hereafter MW81). Although more recent and sophisticated models exist, the MW81 models are simple, accessible, and adequate to demonstrate the points we wish to make. In their Table 1, MW81 presents the extinction optical depths (per 10^{22} H atoms) for separate popula-

tions of silicate and graphite grains, each with a power-law size distribution (following the work of Mathis et al. 1977, hereafter MRN) and six different combinations of the upper and lower grain-size cutoffs, a_+ and a_-, respectively. We produced model extinction curves by summing the graphite and silicate extinction for all possible combinations of the six size distributions (of which there are 36) and three different assumed values for the dust-phase C/Si ratio. As a baseline, we adopt a ratio $(C/Si)_{dust} = 6.5$, which is consistent with the mean for the variety of dust grain models considered by Zubko et al. (2004) and also with mean dust-phase abundances based on solar composition (see, e.g., Table 2.2 of Whittet 2003). We used this value for one set of 36 model optical depth curves and values a factor of 2 lower (3.25) and higher (13) to produce two additional sets. After constructing this ensemble of 108 curves, we converted them from optical depth to absolute extinction and then normalized them by $E(B - V)$, producing curves of $A(\lambda)/E(B - V)$. The justification for producing this multitude of curves is simple: we have no a priori reason to believe that the grain-size distributions must be identical for the graphite and silicate grain populations, as the destruction and, certainly, the growth mechanisms are unlikely to be identical. Furthermore, we do not know the exact abundances of C and Si in the ISM, and suspect that the dust-phase C/Si ratio varies from sight line–to–sight line. Thus our model curves represent a wide range of conditions that may occur in interstellar space.

We seek to compare the shapes of model IR curves with specific $R(V)$ values to the observed parameters determined from Equation (5). Since the MW81 curves are presented at only at a small number of wavelength points, including optical/IR points at B, V, 1.11 μm^{-1} and 0.29 μm^{-1} we take $R(V)$ as the value of $A(\lambda)/E(B - V)$ at the V point and characterize the shape of the IR with a power law fitted through the points at 1.11 μm^{-1} ($\lambda = 0.9$ μm) and 0.29 μm^{-1} ($\lambda = 3.4$ μm), yielding an exponent we refer to as "α_{MW81}." This provides a measure of the general curvature of the extinction between 0 and 1.11 μm^{-1} (i.e., $\lambda > 9000$Å). A fair comparison with the predictions of Equation (5) requires that we compute a similar value of α_{MW81} for each of the curves in Figure 5, using Equation (5) at the same wavelengths.

The comparison between α_{MW81} and $R(V)$ for the models and the observations is shown in Figure 8. Filled circles show the observational results. The distribution of points is similar to that in Figure 6, except that the values of α_{MW81} are ~ 0.15–0.20 smaller than α. Measurement errors were determined in the same way as described above. The theoretical α_{MW81} and $R(V)$ values derived from the 108 model curves are depicted as the x's. The symbol sizes correspond to the (C/Si) ratio in the dust, with $(C/Si)_{dust} = 3.25$, 6.5 and 13 represented by small, medium, and large crosses, respectively. Two interesting points are evident in the figure. First, the main distribution of model points at large $R(V)$ aligns nicely with the "observed" values of $R(V)$ and α_{MW81}. This indicates that the functional form proposed in Equation (5) is compatible with theoretical calculations. Second, there is a group of model points that do not overlap the domain covered by the observations (the models which have small α_{MW81} and small $R(V)$ values). This may indicate that there are specific size distribution and abundance combinations which are not favored by nature. In particular, most of these points arise from the combination of a silicate grain population with a small upper size cutoff ($a_+ = 0.25$) and a graphite grain population with a large upper size cutoff ($a_+ = 0.40$ or 0.50). Note that, because MW81 were explicitly

interested in studying the behavior of curves with large $R(V)$ values, they considered grain size distributions with larger mean sizes than the MRN distribution, which provides a reasonable fit for the Galactic mean curve with $R(V) = 3.1$. As a result, there are no models with large β and small $R(V)$ to compare to the observations. Additional calculations and more sophisticated grain models, such as those discussed by Zubko et al. (2004), will be needed to address this. However, it is the large $R(V)$ sight lines where our results differ most strongly from the paradigm of a universal power law and, in these cases, the comparison in Figure 8 is quite satisfactory.

From the preceding discussion, we conclude that the two parameters needed to fit the observations using Equation (5) are probably the minimum required. This means that the hope of finding a one parameter representation, such as a universal power law with an adjustable $R(V)$ or a model of the sort described by Cardelli et al. (1989), where the curve shape can also have an $R(V)$ dependence, are probably unjustified. We were also able to demonstrate how examining the observed parameters can provide useful constraints on the physical parameters of dust models.

5. SUMMARY AND FINAL COMMENTS

Collecting the results from the previous sections, we have drawn the following conclusions from our analysis of NIR interstellar extinction along 14 sight lines.

1. Our NIR extinction curves can be well represented by a power-law formulation in the I-band through K-band spectral region. However, the exponent of the power law varies significantly from sight line to sight line, which is incompatible with the notion of a universal form to NIR extinction.
2. The value of exponent in the power law, β, is anti-correlated with $R(V)$, showing that the shape of NIR extinction curves are likely functions of the line of sight grain size distributions.
3. The parameters derived from a power-law fit can depend quite strongly on the wavelength interval used to determine them, with the value of β inferred from the fit increasing as longer wavelengths are included. This result demonstrates that extrapolations of power-law fits to longer wavelengths are an unreliable means for estimating $R(V)$.
4. Because of the biases in the power law, we have adopted a different form for the NIR extinction, Equation (4), which has the following properties:
    a) Equation (4) mimics a power law whose exponent increases with wavelength—a property demanded by the power-law analysis.
    b) The four free parameters in Equation (4) can be reduced to two (see Equation (5)), without affecting the quality of the fits to the NIR extinction curves.
    c) For $R(V) \sim 3$, the curve produced by Equation (5) is very similar to the commonly used $\beta = 1.84$ power law.
    d) Equation (5), with its two free parameters, provides better fits to all of the extinction curves than the power-law model which allows the exponent to be a free parameter—giving it three free parameters.
    e) Equation (5) produces $R(V)$ values which are consistent with independent estimates, and are in accord with commonly used methods for estimating $R(V)$.
    f) Unlike the power-law models, Equation (5) gives $R(V)$ values that do not depend strongly or systematically on the wavelength interval used to derive them.
5. For our data, the simple relation $R(V) = -1.36 \frac{E(K-V)}{E(B-V)} - 0.79$ reproduces the $R(V)$ determined from Equation (5) to within ± 0.12, over a large range in $R(V)$. This is a useful relation for estimating $R(V)$ when only limited broadband photometry is available.
6. Using theoretical grain models, we showed that the two parameters needed to fit the observed curves using Equation (5) are probably the minimum required. As a consequence, the notion of finding a one parameter representation, such as a universal power law with an adjustable $R(V)$ or a Cardelli et al. (1989)-like model where the curve shape can also have an $R(V)$ dependence, are probably unjustified.
7. We demonstrated how examining the observed parameters can provide useful constraints on the physical parameters of dust models.

Our results bear heavily on the recent observations of "non-universal" β values noted in Section 1 (i.e., Larson & Whittet 2005; Nishiyama et al. 2006; Froebrich et al. 2007; Gosling et al. 2009) and indicate that they should be viewed with some caution. On the one hand, these may reflect the intrinsic variability expected from an interstellar medium with a wide range in physical properties and grain processing histories for the specific conditions along the respective sight lines. However, care must be taken in comparing β values from different datasets. Our results show that power-law models for a given sight line will yield different exponents, depending on the wavelength range used to derive them. For example, a β-variable power-law fit to Equation (5) in the JHK region gives exponents that are ~ 0.3 larger than those determined by fits which also include the I band. This effect is likely present to some degree in the above studies, which are based solely on JHK data, and should be taken into account before we can obtain an accurate picture of the range in IR extinction properties.

Finally, we point out that while our results are interesting, they are based on only 14 sight lines. Clearly, more NIR data are needed to verify the generality of the constraints placed on Equation (4) to obtain Equation (5), and to verify the relationship $R(V) = -1.36 \frac{E(K-V)}{E(B-V)} - 0.79$.
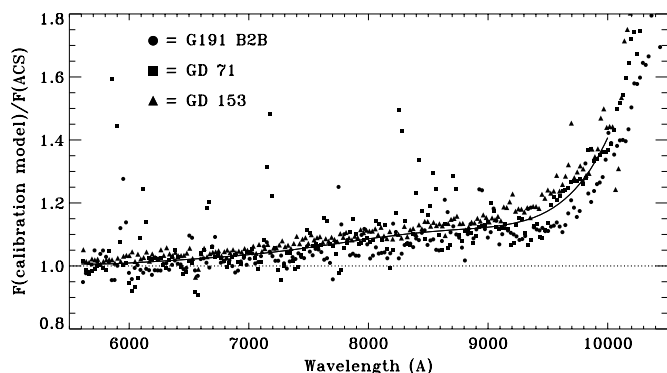
Figure 9. Correction to the ACS/HRC/G800L calibration derived from the three fundamental calibration stars G191 B2B, GD 71, and GD 153.

APPENDIX

ABSOLUTE CALIBRATION OF THE ACS/HRC/ G800L DATA

Because the absolute calibration is critical to our program, we took the additional step to verify the HRC/G800L calibration by processing G800L spectra for three spectrophotometric standard DA white dwarfs (G191B2B, GD 71, and GD 153) used to help establish the fundamental *HST* flux calibration (see, e.g., Bohlin 1996). Our procedure was simple. We downloaded ACS/HRC/G800L spectra for these stars from MAST, processed them in exactly the same manner as our target stars, and then compared the resultant spectra with the model fluxes used to establish the absolute calibration. The models were obtained from the CALSPEC Calibration Database at the Space Telescope Science Institute[7] (the files g191b2b_mod_004.fits, gd71_mod_005.fits, and gd153_mod_004.fits).

Figure 9 shows the results of this comparison. The different symbols show the ratio of the model fluxes to the ACS fluxes as a function of wavelength for each of the three stars. Clearly, the

processed HRC/G800L fluxes are increasingly underestimated at wavelengths longward of ~6000 Å, with the effect increasing dramatically below ~9500 Å. Fortunately, the flux discrepancy is systematic and consistent among the three standards and, thus, can be corrected in a simple way. We derived a correction curve for our processed spectra by fitting a polynomial to the data in Figure 9 and the result is shown as the smooth solid curve in the figure. The systematic scatter of the three stars about the mean correction suggests a zero point stability in the fluxes of ~2.5% at wavelengths shortward of 9500 Å. The variability increases significantly at longer wavelengths. The mean correction in Figure 9 is applied as a multiplicative factor to the calibrated results of the aXe processing.

To perform an independent test of our calibration correction, we examined its effect on the HRC/G800L spectrum of the Galactic O7 star HD 47839 (15 Mon). ACS spectra for HD 47839 were obtained from MAST, and processed in the same way as our program and spectrophotometric calibration stars. Figure 10 shows the multi-wavelength SED of HD 47839 spanning the range ~1150 Å to ~2.2 μm. In the main figure are *IUE* low-resolution UV spectrophotometry ($\lambda \leqslant 3000$ Å), Johnson, Strömgren, and Geneva optical photometry (3300 Å < λ < 6500 Å), and Johnson *RI* and 2MASS *JHK* NIR photometry (λ > 6500 Å). The solid curve is a 37,000 K TLUSTY stellar atmosphere model (Lanz & Hubeny 2003) fitted to the data in the manner described in our previous papers (e.g., Fitzpatrick & Massa 2005a, 2005b). The inset to the figure illustrates the effect of our HRC/G800L correction curve. The smooth curve shows the best fit model while the corrected and uncorrected G800L data are over plotted. The HD 47839 data clearly confirm the results from the analysis of the spectrophotometric standards and the effectiveness of the calibration correction in Figure 9. At wavelengths shortward of 9500 Å the wavelength-dependent signature of the calibration deficiency has been removed and the mean flux level lies about 1% above that predicted by the best-fit SED model, consistent with the scatter among the spectrophotometric standards. At wavelengths longward of 9500 Å, the fluxes are clearly much less reliable.
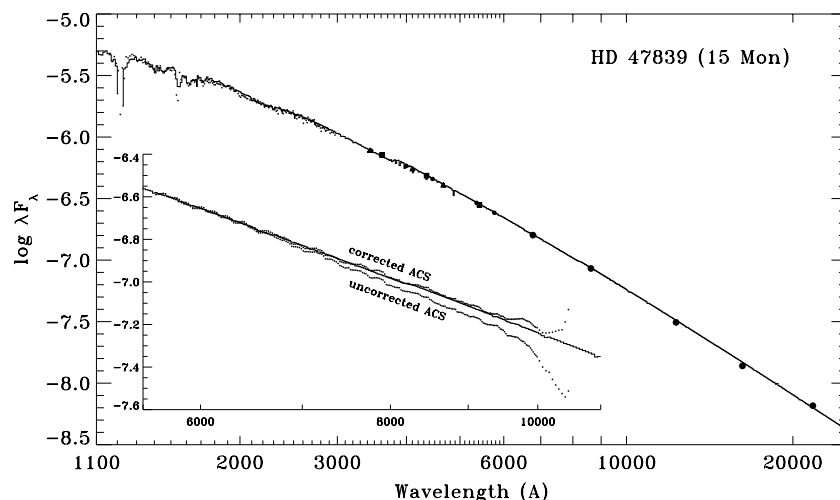
---

[7] http://www.stsci.edu/hst/observatory/cdbs/calspec.html

Figure 10. Verification of the ACS/HRC/G800L calibration correction from Figure 9. The main figure shows the observed SED of HD 47839, including low-resolution *IUE* spectrophotometry (small circles) in the UV (λ < 3000 Å), *UBV* (large circles), Strömgren *uvby* (triangles), and Geneva $UB_1B_2V_1G$ (diamonds) photometry in the optical (3000 Å < λ < 6000 Å), and *RIJHK* photometry in the NIR (λ > 6000 Å). The smooth curve is a 37,000 K TLUSTY model atmosphere (Lanz & Hubeny 2003) fit to the data from (e.g., Fitzpatrick & Massa 2005a, 2005b). The inset illustrates the effect of the ACS/HRC/G800L correction curve shown in Figure 9. It shows the best fit model from the main figure (continuous curve) with the corrected and uncorrected G800L data (points) overplotted. For $\lambda \leqslant 9500$ Å the recalibrated data mimic the shape of the model SED, but lie $\sim$ 1% above it, consistent with the scatter among the spectrophotometric standards. For $\lambda \geqslant 9500$ Å, the fluxes are clearly much less reliable

The calibration correction curve derived in Figure 9 is available from the authors, although it should be noted that is applicable only for first-order HRC/G800L data which are processed using the same aXe parameters as we adopted for our processing, particularly, an extraction window height of ±20 pixels. The methodology is general, however, and it would be a straightforward process to rederive the curve for any combination of processing parameters. Note that we used the same methodology (and the same spectrophotometric standards) to derive corrections to the *IUE* Final Archive calibration (Massa & Fitzpatrick 2000). In addition, our calibration of the optical and NIR photometry (Fitzpatrick & Massa 2005b), which are used in the modeling of the stellar SEDs, was based on these corrected *IUE* results and, therefore, on the HST white dwarf-based fundamental calibration. With the use of the ACS correction derived here, all the data analyzed in this paper are based on an internally consistent absolute calibration.

REFERENCES

Bevington, P. R. 1969, Data Reduction and Error Analysis for the Physical Sciences (New York: McGraw-Hill)
Bohlin, R. C. 1996, AJ, 111, 1743
Cardelli, J. A., Clayton, G. C., & Mathis, J. S. 1989, ApJ, 345, 245
Clayton, G. C., et al. 2003, ApJ, 592, 947
Fitzpatrick, E. L., & Massa, D. 1986, ApJ, 307, 286
Fitzpatrick, E. L., & Massa, D. 1988, ApJ, 328, 734
Fitzpatrick, E. L., & Massa, D. 1990, ApJS, 72, 163
Fitzpatrick, E. L., & Massa, D. 2005a, AJ, 130, 1127
Fitzpatrick, E. L., & Massa, D. 2005b, AJ, 129, 1642

Fitzpatrick, E. L., & Massa, D. 2007, ApJ, 663, 320
Froebrich, D., Murphy, G. C., Smith, M. D., Walsh, J., & Del Burgo, C. 2007, MNRAS, 378, 1447
Gosling, A. J., Bandyopadhyay, R. M., & Blundell, K. M. 2009, MNRAS, 394, 2247
Hecht, J., Helfer, H. L., Wolf, J., Pipher, J. L., & Donn, B. 1982, ApJ, 263, L39
Johnson, H. L. 1968, in Interstellar Extinction (Nebulae and Interstellar Matter. Library of Congress Catalog Card Number 66-13879), ed. B. M. Middlehurst & L. H. Aller (Chicago, IL: Univ. of Chicago Press), 167
Kurucz, R. L. 1991, in NATO ASIC Proc. 341: Stellar Atmospheres: Beyond Classical Models, ed. L. Crivellari, I. Hubeny, & D. G. Hummer (Dordrecht: Reidel), 441
Lanz, T., & Hubeny, I. 2003, ApJS, 146, 417
Larsen, S. S., Kümmel, M., & Walsh, J. R.   2006, in The 2005 HST Calibration Workshop: Hubble After the Transition to Two-Gyro Mode, ed. A. M. Koekemoer, P. Goudfrooij, & L. L. Dressel (Greenbelt, MD: NASA), 103
Larson, K. A., & Whittet, D. C. B. 2005, ApJ, 623, 897
Markwardt, C. B. 2009, arXiv:0902.2850
Martin, P. G., & Whittet, D. C. B. 1990, ApJ, 357, 113
Massa, D., & Fitzpatrick, E. L. 2000, ApJS, 126, 517
Mathis, J. S., Rumpl, W., & Nordsieck, K. H. 1977, ApJ, 217, 425
Mathis, J. S., & Wallenhorst, S. G. 1981, ApJ, 244, 483
Mermilliod, J.-C., Mermilliod, M., & Hauck, B. 1997, A&AS, 124, 349
Nichols, J. S., & Linsky, J. L. 1996, AJ, 111, 517
Nishiyama, S., et al. 2006, ApJ, 638, 839
Pei, Y. C. 1992, ApJ, 395, 130
Rieke, G. H., & Lebofsky, M. J. 1985, ApJ, 288, 618
Spitzer, L. 1978, Physical Processes in the Interstellar Medium (New York: Wiley Interscience)
Walborn, N. R. 1973, AJ, 78, 1067
Whittet, D. C. B. 2003, Dust in the Galactic Environment (Bristol: Institute of Physics Publishing)
Zubko, V., Dwek, E., & Arendt, R. G. 2004, ApJS, 152, 211